HHS Public Access

Author manuscript

J Control Release. Author manuscript; available in PMC 2016 November 10.

Published in final edited form as:

J Control Release. 2015 November 10; 217: 170–182. doi:10.1016/j.jconrel.2015.08.048.

A Radio-Theranostic Nanoparticle with High Specific Drug Loading for Cancer Therapy and Imaging

Andrew B. Satterlee[a], **Hong Yuan**[b], and **Leaf Huang**[a,c,*]

[a]UNC and NCSU Joint Department of Biomedical Engineering, Chapel Hill, NC 27599

[b]Biomedical Research Imaging Center, Department of Radiology, University of North Carolina at Chapel Hill, Chapel Hill, NC 27599-7571

[c]Division of Molecular Pharmaceutics and Center for Nanotechnology in Drug Delivery, Eshelman School of Pharmacy, University of North Carolina at Chapel Hill, Chapel Hill, NC 27599-7571, USA

Abstract

We have developed a theranostic nanoparticle delivering the model radionuclide ^{177}Lu based on the versatile lipid-calcium-phosphate (LCP) nanoparticle delivery platform. Characterization of ^{177}Lu-LCP has shown that radionuclide loading can be increased by several orders of magnitude without affecting the encapsulation efficiency or the morphology of ^{177}Lu-LCP, allowing consistency during fabrication and overcoming scale-up barriers typical of nanotherapeutics. The choice of ^{177}Lu as a model radionuclide has allowed *in vivo* anticancer therapy in addition to radiographic imaging via the dual decay modes of ^{177}Lu. Tumor accumulation of ^{177}Lu-LCP was measured using both SPECT and Cerenkov imaging modalities in live mice, and treatment with just one dose of ^{177}Lu-LCP showed significant *in vivo* tumor inhibition in two subcutaneous xenograft tumor models. Microenvironment and cytotoxicity studies suggest that ^{177}Lu-LCP inhibits tumor growth by causing apoptotic cell death via double-stranded DNA breaks while causing a remodeling of the tumor microenvironment to a more disordered and less malignant phenotype.

Graphical abstract

*Corresponding author. Tel.: 919 843 0736, leafh@unc.edu.

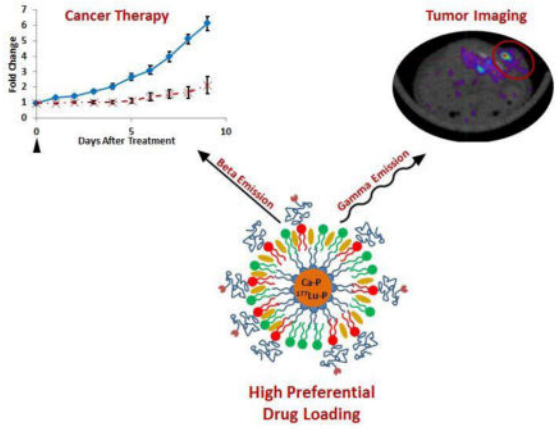

Keywords

Cancer; Theranostic; Nanoparticle; High Specific Drug Loading

Introduction

Standard cancer treatment regimens use combinations of surgery, chemotherapy, and radiation therapy to eradicate the disease. The majority of patients receiving radiation treatments undergo external beam radiation therapy, but systemic internal radiotherapy has also achieved substantial clinical success in the last decade [1]. Unlike external beam therapy, which generally bombards the tumor area with photons or electrons emitted from an external source, systemic radiotherapy targets radionuclides to the tumor site via intravenous injection. The radiation source therefore resides inside the body, and the low radiation emission distance only allows the therapy to affect cells positioned close to particle deposition. This is in contrast to external beam therapy in which x-rays or gamma rays pass through the body from an external source. The current gold standard in systemic radiotherapy, called radioimmunotherapy, chelates the radioisotope to a tumor-targeted monoclonal antibody. The radio-immunotherapeutic Zevalin, which is labeled with the radioisotope ^{90}Yttrium, was the first of its kind, approved by the FDA in 2002 for use against B-cell lymphoma [2], but its clinical success has been tempered because of its high cost and antibody-mediated toxicity [3–5].

In this paper we describe a novel method for systemic internal radiotherapy. We have previously developed a targeted and versatile nanoparticle platform termed Lipid Calcium Phosphate (LCP) [6]. LCP is formulated by mixing two reverse microemulsions containing concentrated calcium and phosphate, and can encapsulate phosphorylated small molecules, peptides, and nucleic acids through their co-precipitation into the amorphous calcium-phosphate precipitate [7–9]. In this report we have now extended the application of this LCP platform by developing a theranostic nanoparticle with high specific drug loading for cancer therapy via the encapsulation of the model radioisotope ^{177}Lutetium (^{177}Lu). Trivalent cations such as lutetium can be driven into LCP, as their solubilities with phosphate are many orders of magnitude lower than the solubility of calcium phosphate. Phosphate then

prefers to precipitate with these radioisotopes and even a trace amount can be encapsulated with high efficiency.

High encapsulation efficiency of a drug is often attainable only when a low amount of drug is loaded into each particle, requiring large doses of the particle to achieve a therapeutic effect. This can cause particle-mediated toxicity and make clinical scale-up very difficult and expensive. Our method of radioisotope loading does not encounter these issues. Because ^{177}Lu can be driven into LCP due to its low solubility with phosphate, and because only a small mass of ^{177}Lu is needed to provide a therapeutic effect, the drug loading window for a batch of LCP can span several orders of magnitude without affecting the ^{177}Lu encapsulation efficiency or LCP morphology, and without requiring a change in any other input parameters.

^{177}Lu was chosen as a model radionuclide because of its ability to provide simultaneous imaging and therapy: γ-radiation from ^{177}Lu is detectible using Single Photon Emission Computed Tomography (SPECT), while β-decay from ^{177}Lu causes DNA damage to nearby cells in addition to inducing Cerenkov radiation that is detectible using optical imaging techniques. Targeted delivery of these radionuclides therefore allows measurement of tumor accumulation in live mice while simultaneously treating the tumor mass. Unlike chemotherapeutics, radioisotopes like ^{177}Lu decay at a constant rate independent of their environment, providing a low, continuous dose to the tumor consistent with their decay rate. We therefore tested the ability of ^{177}Lu-LCP to achieve a sustained and quantifiable therapeutic effect *in vivo* after just a single dose.

Materials and Methods

2.0.1: Materials

$^{177}LuCl_3$ was purchased from PerkinElmer (Waltham, MA). 1,2-dioleoyl-*sn*-glycero-3-phosphate (DOPA), and 1,2-dioleoyl-*sn*-glycero-3-phosphocholine (DOPC) were purchased from Avanti Polar Lipids (Alabaster, AL). N-(Carbonyl-methoxypolyethyleneglycol 2000)-1,2-distearoyl-sn-glycero-3-phosphoethanolamine, sodium salt (DSPE-PEG2000) was purchased by NOF America Corporation (White Plains, NY). DSPE-PEG2000-Anisamide (DSPE-PEG-AA) was synthesized in our lab as described previously [10]. Other chemicals were purchased from Sigma-Aldrich (St. Louis, MO).

2.0.2: Cell Lines

Three different cell lines were used in the experiments described below: NCI-H460 (H460) human non-small cell lung cancer cells, UMUC3 human bladder cancer cells, and NIH/3T3 (3T3) murine fibroblasts. In some experiments, 3T3 cells that had been stably transfected with green fluorescent protein (GFP) were used.

2.0.3: Experimental Animals

6–8 week old female athymic nude mice were used for all experiments presented in this manuscript. These mice were purchased from the National Cancer Institute (Bethesda, MD) and bred at the Division of Laboratory Animal Medicine at the University of North

Carolina-Chapel Hill. All work performed on these animals was approved by the Institutional Animal Care and Use Committee at the University of North Carolina-Chapel Hill.

2.1: ^{177}Lu-LCP Fabrication and Characterization

^{177}Lu-LCP fabrication has been modified [6, 11] from what is described in previous publications. Two reverse microemulsions were prepared in round-bottom flasks. Both microemulsion oil phases contained 73.7:6.7:9.7:10 Cyclohexane:Hexanol:IgepalCO520:TritonX-100 (v:v:v:v). 25mg/ml DOPA was added in chloroform to one oil phase (1:0.023 oil:DOPA v:v). A Phosphate aqueous phase (1:0.0125 oil:aqueous v:v) containing 100mM Na_2HPO_4 in 0.0125M NaOH was added to the DOPA oil phase with stirring. A Calcium aqueous phase containing 500mM $CaCl_2$ and trace $^{177}LuCl_3$ in 0.0125M HCl was added to the other oil phase. After five minutes, the oil phase containing phosphate was added to the oil phase containing calcium and stirred for 40 minutes. 100% ethanol was then added to oil (1:1 ethanol:oil v:v) and stirred for 30 minutes. LCP was washed three times via centrifugation at 12,600g, removing the supernatant, replacing the supernatant with 100% ethanol, and vortexing the solution to resuspend the LCP pellet. Lu, Ca, and PO_4 that had not precipitated during mixing were discarded in the supernatant of the initial wash (~15% of input ^{177}Lu was removed here), and minimal ^{177}Lu signal was detected in the second and third supernatants. After the final wash, the precipitate was dissolved in chloroform and centrifuged at 10,000g for five minutes. This supernatant then contained the organic-soluble LCP cores, and the pellet contained any precipitate that was not well-coated in DOPA, and therefore not soluble in chloroform (~15% of input ^{177}Lu was removed here). Purifying the LCP cores in these two ways ensured that ^{177}Lu was only present inside the LCP. Outer leaflet lipids (OLLs) dissolved in chloroform were then added to the chloroform-soluble cores (40:40:18:2 DOPC:cholesterol:DSPE-PEG2000:DSPE-PEG2000-AA mol:mol:mol) (0.11:1 total OLL:initial oil phase v:v; all lipids at 20mM concentration). In experiments using DiI-labeled LCP, DiI dissolved in chloroform was added to the cores with the OLLs (1:100 DiI:total OLL mol:mol). Chloroform was evaporated until the particles and lipids coated the vial in a lipid film. Particles were then rehydrated with 80°C water to the injection volume. The solution was vortexed and sonicated liberally, then heated at 80°C for >10 min and passively cooled. The anisamide ligand was used in all formulations to target the sigma receptor overexpressed in UMUC3 and H460 cells [12, 13].

In experiments using DiI-labeled Lu-LCP, sucrose gradient ultracentrifugation (50,000g for 4 h) was used to purify DiI-Lu-LCP from excess free DiI and DiI that had incorporated into excess free liposomes. Encapsulation efficiency of ^{177}Lu into ^{177}Lu-LCP was measured by a Model AA2010 “Nucleus” Gamma Scintillation Counter or a Capintec Radioisotope Calibrator CRC-127R and calculated as (signal from ^{177}Lu in LCP cores)/(signal from ^{177}Lu in input aqueous phase). ^{177}Lu-LCP hydrodynamic diameter and zeta potential were measured after sucrose gradient ultracentrifugation using a Malvern Nano ZS dynamic light scattering instrument. Three different batches of LCP were measured. Particle size was corroborated using transmission electron microscopy (TEM).

2.2: Loading Capacity

To simulate an increase in ^{177}Lu loading into ^{177}Lu-LCP, a trace amount of ^{177}Lu was supplemented with additional nonradioactive ^{175}Lu. As the Lu:Ca input ratio was increased from 1:10,000,000 to 1:1, no changes in any inputs were made save for the increase in ^{175}Lu. ^{177}Lu EE was measured using gamma scintillation and ^{177}Lu-LCP morphologies/structural makeups were measured using TEM and energy-dispersive X-ray spectroscopy (EDS) at the Chapel Hill Analytical and Nanofabrication Laboratory at the University of North Carolina at Chapel Hill. TEM images were taken using a TEM JEOL 2010F-FasTEM or a TEM JEOL 100CX II, and EDS measurements were taken using the TEM JEOL 100CX II.

2.3: Pharmacokinetics and Biodistribution

Healthy nude mice were injected with ^{177}Lu-LCP or free $^{177}LuCl_3$ of known activities. The ^{177}Lu-LCP or $^{177}LuCl_3$ was injected into the left tail vein and circulating ^{177}Lu-LCP or $^{177}LuCl_3$ was measured by removing 20–30 μl of blood from the right tail vein at several time points after injection. The signal was read using gamma scintillation and was used to calculate the total signal remaining in the blood. A Microsoft Excel Add-In called PKSolver [14] was used for the pharmacokinetic analysis. In a separate experiment, H460 or UMUC3/3T3 tumor-bearing mice were injected with a therapeutic dose of ^{177}Lu-LCP or free $^{177}LuCl_3$. Twenty four h after injection, the mice were sacrificed and their organs were dissected and read for ^{177}Lu activity.

2.4: SPECT and Cerenkov Imaging

UMUC3/3T3 tumor-bearing nude mice were i.v. injected with 2.5 mCi of ^{177}Lu-LCP or free $^{177}LuCl_3$. Twenty four h later, the mice were imaged using a small animal SPECT/CT system (eXplore speCZT, GE Healthcare) at the Small Animal Imaging facility on the UNC campus. SPECT Images were taken with the energy window to be set from 188–229 keV to receive the main gamma photon from Lu-77 peaked at 208 keV. A mouse slit collimator was used to provide whole body imaging with 1.5mm transaxial and 2.5mm axial resolution, and a pinhole collimator was used for partial body imaging with higher resolution (1mm isotropic resolution). Immediately after SPECT/CT imaging, the mice were taken to an *in vivo* optical imaging system (IVIS-Kinetic, Perkin Elmer) to measure Cerenkov emissions generated by ^{177}Lu.

2.5: *In Vivo* Tumor Inhibition

Six to eight week old nude mice were subcutaneously inoculated with 100ul PBS containing 5×10^6 H460 cells or 5×10^6 UMUC3 cells + 2.5×10^6 3T3 cells in 25% matrigel (BD matrigel matrix high concentration) on the left flank. After 8–12 days, when tumors had reached a size of 100–150mm^3, mice were given a single injection of PBS (Untreated mice), non-radioactive (cold) ^{175}Lu-LCP, free radioactive $^{177}LuCl_3$, or radioactive ^{177}Lu-LCP. Mice bearing UMUC3/3T3 tumors received a dose of 200 μCi/mouse and mice bearing H460 tumors received a dose of 250 μCi/mouse. Mouse weight was measured every 2 days until untreated mice reached humane endpoints. Tumor volume was measured with digital

calipers and calculated as (L x W x D)/2. n = 5–8. Student's t-test of the final AUC used for statistical analysis.

2.6 Tumor Accumulation

Nude mice bearing s.c. H460 or UMUC3/3T3 tumors were treated with one dose of 250 μCi or 200 μCi ^{177}Lu-LCP, respectively, or appropriate controls. The lipid bilayer of the ^{177}Lu-LCP particles were labeled with the fluorescent small molecule DiI to allow LCP measurement in the tumor. Twenty four h after injection, mice were sacrificed and tumors were dissected and cut in half. One half was frozen in OCT, sectioned, and mounted for DiI Lu-LCP imaging, and the other half was fixed in 4% formalin, embedded in paraffin, and sectioned for CD-31 staining (1:100 dilution rabbit primary Ab, Abcam #ab28364; 1:100 dilution anti-rabbit 647 fluorescent secondary Ab, Cell Signaling #4414) and DAPI counterstain.

2.7 Cytotoxicity Studies

One, 2, and 4 days after treatment with 200 μCi ^{177}Lu-LCP or controls, UMUC3/3T3 tumor-bearing nude mice were sacrificed and their tumors were dissected, fixed, and sectioned in paraffin. Adjacent sections were stained for p-H2AX immunofluorescence (1:100 dilution Rabbit monoclonal primary Ab, Cell Signaling #9718; 1:100 dilution anti-rabbit 647 fluorescent secondary Ab, Cell Signaling #4414) and Terminal deoxynucleotidyl transferase dUTP nick end labeling (DeadEnd™ Fluorometric TUNEL System, Promega) with DAPI counterstains.

2.8 Microenvironment Studies

Nude mice were inoculated with UMUC3/3T3-GFP (fluorescent) tumors using the same cell numbers reported above. When tumors reached ~400 mm^3, mice were treated with 200 μCi of fluorescently labeled DiI-^{177}Lu-LCP or controls. After 2 days, mice were sacrificed and their tumors were dissected and prepared for freezing in OCT via a 2-h fixation in 4% formalin followed by overnight incubation in a 30% sucrose solution at 4°C. The frozen tumors were sectioned and imaged with DAPI counterstain to measure GFP and DiI distribution. DiI distribution was quantified using Matlab.

Separate nude mice were inoculated with UMUC3/3T3 (nonfluorescent) tumors. When tumors reached ~300 mm^3, mice were treated with 200 μCi of ^{177}Lu-LCP or controls. Four days after treatment, the tumors were dissected, fixed, and sectioned in paraffin. Adjacent sections were trichrome stained and stained for α-SMA immunofluorescence (1:100 dilution Rabbit monoclonal primary Ab, Abcam #ab5694; 1:100 dilution anti-rabbit 647 fluorescent secondary Ab, Cell Signaling #4414) with DAPI counterstain. The stained sections were digitally scanned using the Aperio Scanscope at the University of North Carolina-Chapel Hill's Translational Pathology Lab. Quantitative analysis was performed on Imagescope and ImageJ software.

2.9: Toxicity Studies

Nude mice and CD-1 mice were treated with 250 μCi of ^{177}Lu-LCP or appropriate controls and were sacrificed 12 days after treatment. Blood and organs were dissected. Serum levels

of AST, ALT, BUN, and creatinine were measured, and organs were stained with H&E to measure any changes in tissue morphology. Whole blood was measured for changes in white blood cell count (WBC), hematocrit (HCT), mean cell volume (MCV), red blood cell count (RBC), hemoglobin count (HGB), and platelet count (PLT).

Results

3.1: Lu-LCP Fabrication and Characterization

The LCP nanoparticle platform preferentially encapsulates ^{177}Lu in its solid amorphous calcium phosphate core during fabrication (Scheme shown in Figure 1A). Just a trace amount of ^{177}Lu can be efficiently encapsulated because of lutetium's much lower solubility with phosphate ($k_{sp} = 2\times10^{-25}$) [15] when compared to calcium's solubility with phosphate ($k_{sp} = 1\times10^{-7}$). The fabrication protocol for ^{177}Lu-LCP was modified [6, 11] from previous publications to maximize ^{177}Lu encapsulation efficiency (EE) at approximately 70%, with the majority of the loss occurring during washing and purification. Particles were measured via dynamic light scattering to have a diameter of 36 ± 9 nm and a polydispersity index of 0.27 ± 0.05, with a zeta potential of −6.7 ± 3.5 mV after separating the particles from excess empty liposomes using sucrose gradient centrifugation (Supplemental Table S1). Particle size was corroborated by transmission electron microscopy (Figure 1B–C). Although cellular entry is not requisite for ^{177}Lu-LCP to achieve therapeutic effect, because anisamide has been proven as an effective targeting ligand against the sigma receptor overexpressed in epithelial cancers such as UMUC3 and H460 [12, 13], and because receptor-mediated endocytosis draws nanoparticles inside the cell and closer to nuclear DNA, DSPE-PEG-Anisamide was exclusively used in all Lu-LCP formulations as described in section 2.1 to provide the greatest statistical chance for treatment efficacy.

3.2: Loading Capacity

Preferential loading of ^{177}Lu allows ^{177}Lu-LCP to be fabricated with a very high radioisotope concentration, consequently allowing very high drug loading in a particle that is still overwhelmingly comprised of calcium phosphate. Figure 2 and Table 1 show that the drug loading window in equivalent-sized batches of LCP core spans across several orders of magnitude without affecting the ^{177}Lu encapsulation efficiency and not requiring a change in any other input parameters. Additionally, the LCP morphology remains unchanged up to a Lu:Ca input ratio of 1:1000 (Figure 3A–F), above which the Lu starts becoming a structural component of the LCP, as measured by EDS (Figure 3G), which introduces heterogeneity to the formulation. As Lu:Ca is increased to 1:1, Lu forces out nearly all Ca from the LCP to form cores of $LuPO_4$, but the total dose of heavy metal per particle is undesirable due to its inherent toxicity. These data suggest that the maximum Lu:Ca input ratio that maintains desirable encapsulation and morphology is 1:1000. At this input ratio, ~24 mCi of ^{177}Lu—enough to treat over 100 mice—can be encapsulated in a batch size of only 3.2 total mL of oil phase. Considering that it is not uncommon for other types of LCP formulations to be synthesized in batches of 120ml or more for small mouse studies, one can understand how Lu-LCP is able to avoid scale-up complications generally associated with nanoparticles. Moreover, a very small mass of total lutetium—approximately 70 pmol/mouse, or 6×10^{-4} mg/kg—is used here to achieve therapeutic effect. This low total dose is important in

minimizing heavy metal-mediated toxicity. Combined, the high drug loading window and low total mass of lutetium in ^{177}Lu-LCP minimize batch size and toxicity while subsequently allowing the treatment of a large number of animals per batch.

3.3: Pharmacokinetics and Biodistribution

The pharmacokinetics and biodistribution of ^{177}Lu-LCP were determined in tumor-bearing nude mice. A two-compartment model [14] was used to calculate the clearance half-lives, which were 0.52 h for the distribution half-life, $t_{1/2}\alpha$, and 7.28 h for the elimination half-life, $t_{1/2}\beta$, as shown in Figure 4A. Pharmacokinetic analysis was also performed for free $^{177}LuCl_3$, which showed nearly 80% blood clearance in the first 30 min after injection (Figure S1). It can therefore be concluded that the circulating signal from mice given ^{177}Lu-LCP is indeed from intact particles. The biodistribution of ^{177}Lu-LCP and free ^{177}Lu in tumor-bearing mice is given in Figure 4B. ^{177}Lu-LCP shows significant accumulation in the tumor, as well as accumulation in the nanoparticle clearing organs, the liver and spleen, as it is too large to clear renally. In contrast, free ^{177}Lu is an ion that is plenty small to clear through the kidneys, but also selectively accumulates in the bones, as lanthanide elements are known to do [16]. Free ^{177}Lu also shows some kidney accumulation, which may occur during the quick renal clearance of the element (Figure 4B).

3.4: SPECT and Cerenkov Imaging

In addition to allowing simple means of detection using gamma scintillation, ^{177}Lu can also be used as a SPECT contrast agent, permitting measurement of ^{177}Lu biodistribution and tumor accumulation in live mice. Figure 5A–E shows the biodistribution of ^{177}Lu-LCP 24 h after injection, including the visible accumulation of ^{177}Lu in the tumor. In contrast, free $^{177}LuCl_3$ does not accumulate in the tumor and therefore tumor accumulation is not visible using SPECT/CT imaging (Figure 5F–H).

Interestingly, ^{177}Lu also allows imaging via its β-emissions, which are the same decay products (electrons) that induce its therapeutic effect. As the β-particles move through the tissue over their average path length of ~250 μm, they induce photon emissions from the medium with energies in the visible spectrum. This so-called Cerenkov light was measured using an *in vivo* optical imaging system (Figure 6), also showing tumor uptake of ^{177}Lu-LCP and corroborating the results obtained during SPECT/CT imaging. Cerenkov imaging is a particularly interesting imaging modality because it offers a less expensive and more convenient alternative to SPECT that is not generally used in this field. Although its spatial resolution and depth of penetration is not as high as SPECT or PET, Cerenkov imaging uses less expensive hardware and requires acquisition times of only a few seconds, if the radioisotope and dose are adequate.

After imaging was complete, the mouse organs were dissected and their ^{177}Lu signal was read using gamma scintillation. These values are shown in Supplementary Table S2.

3.5: *In Vivo* Tumor Growth Inhibition

To assess the effectiveness of a single treatment of ^{177}Lu, one dose of ^{177}Lu-LCP was intravenously injected into two different subcutaneous xenograft tumor models. One of the

models was an aggressive stroma-rich human bladder cancer model previously developed by our lab. This model uses both UMUC3 bladder cancer cells and NIH-3T3 fibroblasts to generate a tumor that has been shown to be more similar to patient bladder cancer than UMUC3 tumors alone [17]. As shown in Figure 7A, a single 200 μCi dose of ^{177}Lu-LCP showed sustained and significant tumor growth inhibition compared to tumors treated with nonradioactive ^{175}Lu-LCP and tumors receiving only free $^{177}LuCl_3$. ^{177}Lu-LCP was also tested on the aggressive and radio-resistant [18] H460 human non-small cell lung cancer model; an increased dose of 250 μCi of ^{177}Lu-LCP provided statistically significant tumor growth inhibition as shown in Figure 7B. This boosted dose was still low enough to avoid changes in mouse body weight (Figure S2), and the accumulated dose over the course of the study did not significantly elevate liver/kidney toxicity markers (Table 2).

3.6: Tumor Accumulation

To compare the localization of ^{177}Lu-LCP inside H460 and UMUC3/3T3 tumors, the fluorescent small molecule DiI was incorporated into the outer leaflet of the nanoparticle. DiI has been widely used in liposomal formulations and as a cell membrane marker, and is well known to faithfully remain in the hydrophobic portion of the lipid bilayer [19, 20]. Tumor-bearing mice were sacrificed 24h after injection with DiI-labeled ^{177}Lu-LCP, and tumor sections were imaged for DiI uptake. Figure S3A shows that the bladder cancer tumor has more homogeneous uptake of particles when compared to the H460 lung cancer tumor. This could be because the bladder cancer tumors contain more CD-31-positive area than the H460 tumors (Figure S3B), corresponding to more vasculature. This could also explain the greater tumor accumulation of ^{177}Lu-LCP in the UMUC3/3T3 tumors shown in Figure 4B. The UMUC3/3T3 bladder cancer tumor model was therefore chosen for more detailed mechanistic analysis.

3.7: Mechanisms of Tumor Growth Inhibition: Cytotoxicity Studies

While many chemotherapeutic therapies and treatments using external radiation require multiple doses to generate therapeutic effect, just one dose of ^{177}Lu-LCP provides continuous treatment of the tumor as the ^{177}Lu slowly decays, leading to sustained tumor growth inhibition for several days. We desired to investigate the mechanisms by which this sustained effect occurs, and hypothesized that the cytotoxic β-emissions from ^{177}Lu would persistently induce double-stranded DNA breaks. To study this phenomenon, we looked further into the stroma-rich bladder cancer tumor model. Mice were sacrificed one, two, and four days after treatment with 200 μCi of ^{177}Lu-LCP or appropriate controls. Immunofluorescent staining for p-H2AX, a protein that is phosphorylated in response to DNA double-stranded breaks [21], showed that the maximum induction of the protein occurred two days after treatment and remained elevated even four days after treatment (Figure 8A). This DNA damage led to cell death via apoptotic fragmentation of DNA, which was most induced four days after treatment as measured through the TUNEL assay (Figure 8B). This suggests that the cumulative dose of radiation from ^{177}Lu-LCP causes maximum DNA damage after ~48 h, and this damage translates to apoptotic cell death shortly thereafter. ^{177}Lu-LCP induces significantly higher maximum H2AX phosphorylation and cell death than free ^{177}Lu ($p<0.05$), and the difference in the pattern of cytotoxic effects between these two treatments may be due to a difference in pharmacokinetics/dynamics, as

free ^{177}Lu quickly clears from circulation and may deposit into the tumor much earlier, more transiently, and with a different intratumoral distribution than ^{177}Lu-LCP.

3.8: Mechanisms of Tumor Growth Inhibition: Microenvironment Studies

Changes in the tumor microenvironment were observed as well: Figure 9 shows that a diffuse and disordered fibroblast structure was present two days after treatment with ^{177}Lu-LCP, in contrast to the organized fibroblast structure present in untreated and control-treated tumors of the same size (see higher magnification images in Figure 9 D–E). These images clearly show that the fibroblasts in untreated tumors can organize into a defined morphology to form tumor nests, while those fibroblasts in tumors that have been treated with ^{177}Lu-LCP are dispersed and without this mature organization. Four days after treatment, the disorganized fibroblast structure persisted (Figure 10 A–D), along with changes in the collagen structure in the tumor, in which the long swaths of collagen in the untreated tumor had been replaced with shorter and more tortuous collagen fibers (Figure 10 E–H). It is known that the organized fibroblast structure and more ordered, linearized, and bundled collagen fibers present in the untreated tumor are associated with a more mature and malignant phenotype, while a disordered fibroblast structure with short, tortuous collagen fibers like those of the treated tumor suggest a tumor microenvironment less structurally and functionally capable of growth and progression [22–26].

We also desired to measure the intratumoral localization of Lu-LCP. Unlike traditional chemotherapeutics that must enter the target cell in order to impart their therapeutic effect, internal radiotherapy can damage cells at a distance several cell lengths from the source. β-particles from ^{177}Lu, for example, have a maximum energy of ~500 keV, allowing an average path length in tissue of 200–300 μm [27] and a maximum path length of ~4x that value [28]. ^{177}Lu-LCP may then be able to provide therapeutic effect to cells that did not take up the particles, which is especially important given the intratumoral heterogeneity of nanoparticle delivery in general. We supposed that a majority of cells in a tumor would be “in range” for β-particle damage after ^{177}Lu-LCP distribution, but desired to measure the intratumoral localization of ^{177}Lu-LCP in order to calculate this important spatial relationship between cells and particles. The lipid membrane of the LCPs used in the experiment described in Figures 10 and 12 were labeled with fluorescent DiI, and excess DiI was purified away using sucrose gradient centrifugation in order to measure the dispersion of the particles throughout the tumor. Tumor sections from several areas in different tumors were then analyzed to quantify distances between cells and nanoparticles. Figure 11 shows that nearly 100% of cells in the field are within just 50 μm of the nearest Lu-LCP, well within the average path length of a β particle, even though the only nanoparticles considered are those present in that 2-D plane—Lu-LCPs residing in the z-direction would only increase the particles in range for a given cell. This substantiates the claim that although not all tumor cells have taken up particles, all are susceptible to the delivered therapeutic payload.

3.9: Toxicity Studies

To gauge the cumulative toxicity of ^{177}Lu-LCP in mice, we treated healthy immunocompromised nude mice and healthy immunocompetent CD-1 mice with a single

dose of 250 μCi of ^{177}Lu-LCP, the highest dose used in this study. Mice were sacrificed 12 days after treatment to assess the cumulative effect of the radiation. At the conclusion of the 12-day study, mouse organs were dissected and sectioned, serum markers for kidney and liver toxicity were measured (ALT, AST, BUN, and creatinine), and whole blood from the immunocompetent CD-1 mice was analyzed for changes in white blood cell count (WBC), hematocrit (HCT), mean cell volume (MCV), red blood cell count (RBC), hemoglobin count (HGB), and platelet count (PLT). These results were compared against appropriate controls and against the normal range for these values. Morphologies of kidney, liver, heart, lung, skin, and small intestine sections after H&E staining showed no difference from normal tissue in nude mice (Figure 12) or in CD-1 mice (Figure S4). Serum markers for renal and hepatotoxicity also remained in the normal range in both nude and CD-1 mice (Table 2A–B) after treatment. The data do show some well-tolerated side effects as a result of this treatment, including differences in spleen morphology as well as a decrease in white blood cell and platelet counts outside the normal range. Hematological side effects are common during cancer therapy and are easily handled using immune boosters, etc., which were not used in this study. None of these side effects translated to a decrease in mouse body weight (Figure S2).

Discussion

In this paper, we have described a novel method for systemic internal radiotherapy by extending the anticancer application of our LCP platform to include a theranostic nanoparticle with high specific drug loading. The preferential uptake of ^{177}Lu into LCP allows a huge amount of ^{177}Lu to be encapsulated in a very small batch of particles without changing the LCP's morphology or encapsulation efficiency. The difficulty of nanoparticle scale-up that is pervasive throughout this field is therefore eliminated, as a therapeutic dose for a mouse or a human can be made on the same benchtop.

The theranostic advantage of radioisotope loading into LCP should also not be understated. ^{177}Lu's γ emissions permitted live *in vivo* imaging using SPECT to measure tumor accumulation of ^{177}Lu-LCP, paving the way for future delivery to orthotopic tumors that will represent a more clinically relevant "diagnostic" procedure. The β decay from ^{177}Lu also causes significant tumor inhibition via DNA double-stranded breaks while simultaneously inducing Cerenkov radiation for imaging. Because therapeutic β-emissions are also the imaging contrast agent, Cerenkov imaging is a wonderful example of a theranostic application. Compared to SPECT, Cerenkov imaging correctly estimated the general biodistribution of ^{177}Lu-LCP at a fraction of the time and cost. This opens up opportunity for several applications such as dynamically looking at early stages of biodistribution and clearance by taking many images in quick succession. Because the high loading of Lu into LCP is broadly applicable to several other polycationic radiometals, such as the β-emitter and effective Cerenkov agent ^{90}Y, it is worthwhile to discuss Cerenkov imaging as an interesting and useful theranostic application.

As a follow-up to our tumor inhibition data, we were interested in assessing any significant changes in the tumor microenvironment as a result of this treatment, and we evaluated these changes by measuring the fibroblast and collagen structure in the tumor. The changes in the

tumor microenvironment may be explained by looking deeper into how β-radiation causes the double-stranded DNA breaks that are shown to be elevated in the treated tumors. Generally, β-radiation is classified as having low linear energy transfer (LET); that is, the β-particles deposit a small fraction of their energy per unit length as they travel along their path [28]. In most cases, the DNA damage does not occur via direct interaction between a DNA strand and the β-particle itself. In the case of low LET emitters like ^{177}Lu, it is known that most DNA damage is caused by an increase in reactive oxygen species (ROS) generated as the emitted β-particles interact with and radicalize water molecules along their path. The induced ROS then damage DNA and cause single and double-stranded breaks in an “indirect radiation effect” [28].

Oxidative stress is known to cause many changes in the cellular and extracellular environment, especially in rapidly remodeling tissues like cancer, where actin and collagen are just some of the proteins susceptible to oxidative damage [29–33]. Actin is an important structural component of cells and is also a structural player in the adherens junctions between 3T3 fibroblasts [34]. The cysteine residues on actin are susceptible to oxidative damage, and this damage can prevent polymerization, cause depolymerization, and affect the organization of actin in cells, potentially restricting the organization of fibroblasts in the tumor. Collagen stability is also affected by oxidative damage, as scissions in the collagen α-bands can decrease the degradation temperature of the collagen to below body temperature and prevent the formation of collagen fibrils [30, 31]. These results suggest that cumulative ROS damage may cause the observed changes in the overall *in vivo* collagen and fibroblast structure shown in Figures 10 and 11, prohibiting the dynamic formation of bundled collagen and organized fibroblast structures that have been implicated in the formation of resistant tumor nests found in more advanced and aggressive tumors.

Tumor growth inhibition via ^{177}Lu-LCP may then occur by taking advantage of both the uncontrolled growth and the excessive microenvironment remodeling observed in cancer. The low, continuous dose of radiation damages tumor cell DNA that can have fewer active repair mechanisms and divide much more rapidly than healthy cells while inhibiting the progression of the microenvironment toward malignancy. This allows sustained cancer treatment at a dose that preserves the health of the subject.

Part of the beauty of this approach to radioisotope loading is its broad application for many trivalent radiometals, such as other therapeutic radionuclides like ^{90}Y or ^{192}Ir, which are great candidates for future work in this subject. Combination therapy using a radiotherapeutic and a radiosensitizing chemotherapeutic residing in the same LCP particle should also be possible, given that many small molecule drugs have previously been encapsulated in LCP.

Future work should also investigate whether systemic administration of a radiotherapeutic LCP is the most effective dosing method. Macro and micro-dosimetric calculations should be used to determine absorbed doses in the mouse and how the distribution of nanoparticles necessitates different calculations than doses from an external beam. In one potential local delivery scenario, highly loaded ^{177}Lu-LCP, ^{192}Ir-LCP, or ^{90}Y-LCP could be directly injected into prostate tumors to create a sort of nano-brachytherapy, in which modified

particles would disseminate locally and stably in the prostate but remain out of the systemic circulation.

Conclusions

Radionuclide loading into ^{177}Lu-LCP can be increased by several orders of magnitude without affecting the ^{177}Lu encapsulation efficiency or LCP morphology, generating a nanoparticle with high radioisotope concentration that overcomes scale-up barriers typical of nanotherapeutics and minimizes heavy metal-based toxicities. The choice of ^{177}Lu as a model radionuclide has allowed *in vivo* anticancer therapy via DNA damage and microenvironment remodeling, in addition to permitting live animal SPECT/CT and Cerenkov imaging. As studies in LCP-mediated radionuclide therapy continue, other nuclides may be considered, perhaps in combination with chemotherapeutics, for several different therapeutic approaches.

Supplementary Material

Refer to Web version on PubMed Central for supplementary material.

Acknowledgments

ABS was supported by the National Science Foundation's Graduate Research Fellowship Program. We thank the Small Animal Imaging facility, especially staff Kevin Guley and Joseph Merrill, at the UNC Biomedical Imaging Research Center for providing the SPECT/CT and Cerenkov imaging service. The imaging core is supported in part by NCI Grant #P30-CA016086-35-37. The work was supported by NIH grants CA149363, CA151652 and CA149387.

Abbreviations

AA	Anisamide
DOPA	1,2-dioleoyl-*sn*-glycero-3-phosphate
DOPC	1,2-dioleoyl-*sn*-glycero-3-phosphocholine
DSPE-PEG2000	N-(Carbonyl-methoxypolyethyleneglycol 2000)-1,2-distearoyl-sn-glycero-3-phosphoethanolamine, sodium salt
EDS	Energy-Dispersive X-ray Spectroscopy
EE	Encapsulation Efficiency
K_{sp}	Solubility Product Constant
LCP	Lipid-Calcium-Phosphate
Lu	Lutetium
SPECT	Single Photon Emission Computed Tomography
TEM	Transmission Electron Microscopy

References

1. Goldsmith SJ. Radioimmunotherapy of lymphoma: Bexxar and Zevalin. Semin Nucl Med. 2010; 40(2):122–35. [PubMed: 20113680]
2. Grillo-Lopez AJ. Zevalin: the first radioimmunotherapy approved for the treatment of lymphoma. Expert Rev Anticancer Ther. 2002; 2(5):485–93. [PubMed: 12382517]
3. van der Kolk LE, et al. Complement activation plays a key role in the side-effects of rituximab treatment. Br J Haematol. 2001; 115(4):807–11. [PubMed: 11843813]
4. Kulkarni HS, Kasi PM. Rituximab and cytokine release syndrome. Case Rep Oncol. 2012; 5(1): 134–41. [PubMed: 22666201]
5. Rezvani AR, Maloney DG. Rituximab resistance. Best Pract Res Clin Haematol. 2011; 24(2):203–16. [PubMed: 21658619]
6. Li J, Yang Y, Huang L. Calcium phosphate nanoparticles with an asymmetric lipid bilayer coating for siRNA delivery to the tumor. J Control Release. 2012; 158(1):108–14. [PubMed: 22056915]
7. Zhang Y, et al. Codelivery of VEGF siRNA and gemcitabine monophosphate in a single nanoparticle formulation for effective treatment of NSCLC. Mol Ther. 2013; 21(8):1559–69. [PubMed: 23774791]
8. Zhang Y, et al. Combinational delivery of c-myc siRNA and nucleoside analogs in a single, synthetic nanocarrier for targeted cancer therapy. Biomaterials. 2013; 34(33):8459–68. [PubMed: 23932296]
9. Hu Y, et al. A highly efficient synthetic vector: nonhydrodynamic delivery of DNA to hepatocyte nuclei in vivo. ACS Nano. 2013; 7(6):5376–84. [PubMed: 23647441]
10. Banerjee R, et al. Anisamide-targeted stealth liposomes: a potent carrier for targeting doxorubicin to human prostate cancer cells. Int J Cancer. 2004; 112(4):693–700. [PubMed: 15382053]
11. Tseng YC, et al. Lipid-calcium phosphate nanoparticles for delivery to the lymphatic system and SPECT/CT imaging of lymph node metastases. Biomaterials. 2014; 35(16):4688–98. [PubMed: 24613050]
12. Miao L, et al. Nanoparticles with Precise Ratiometric Co-Loading and Co-Delivery of Gemcitabine Monophosphate and Cisplatin for Treatment of Bladder Cancer. Adv Funct Mater. 2014; 24(42): 6601–6611. [PubMed: 25395922]
13. Zhang Y, Kim WY, Huang L. Systemic delivery of gemcitabine triphosphate via LCP nanoparticles for NSCLC and pancreatic cancer therapy. Biomaterials. 2013; 34(13):3447–58. [PubMed: 23380359]
14. Zhang Y, et al. PKSolver: An add-in program for pharmacokinetic and pharmacodynamic data analysis in Microsoft Excel. Comput Methods Programs Biomed. 2010; 99(3):306–14. [PubMed: 20176408]
15. Byrne, XLaRH. Rare earth and yttrium phosphate solubilities in aqueous solution. Geochimica et Cosmochimica Acta. 1997; 61(8):1625–1633.
16. Zaichick S, et al. Accumulation of rare earth elements in human bone within the lifespan. Metallomics. 2011; 3(2):186–94. [PubMed: 21173982]
17. Zhang J, et al. Synergistic anti-tumor effects of combined gemcitabine and cisplatin nanoparticles in a stroma-rich bladder carcinoma model. J Control Release. 2014; 182:90–6. [PubMed: 24637468]
18. Torres-Roca JF, et al. Prediction of radiation sensitivity using a gene expression classifier. Cancer Res. 2005; 65(16):7169–76. [PubMed: 16103067]
19. Honig MG, Hume RI. Dil and diO: versatile fluorescent dyes for neuronal labelling and pathway tracing. Trends Neurosci. 1989; 12(9):333–5. 340–1. [PubMed: 2480673]
20. Guo S, et al. Lipid-coated Cisplatin nanoparticles induce neighboring effect and exhibit enhanced anticancer efficacy. ACS Nano. 2013; 7(11):9896–904. [PubMed: 24083505]
21. Rogakou EP, et al. DNA double-stranded breaks induce histone H2AX phosphorylation on serine 139. J Biol Chem. 1998; 273(10):5858–68. [PubMed: 9488723]
22. Ingber DE. Can cancer be reversed by engineering the tumor microenvironment? Semin Cancer Biol. 2008; 18(5):356–64. [PubMed: 18472275]

23. Provenzano PP, et al. Collagen reorganization at the tumor-stromal interface facilitates local invasion. BMC Med. 2006; 4(1):38. [PubMed: 17190588]
24. Cox TR, Erler JT. Remodeling and homeostasis of the extracellular matrix: implications for fibrotic diseases and cancer. Dis Model Mech. 2011; 4(2):165–78. [PubMed: 21324931]
25. Baglole CJ, et al. More than structural cells, fibroblasts create and orchestrate the tumor microenvironment. Immunol Invest. 2006; 35(3–4):297–325. [PubMed: 16916756]
26. Clark AK, et al. A bioengineered microenvironment to quantitatively measure the tumorigenic properties of cancer-associated fibroblasts in human prostate cancer. Biomaterials. 2013; 34(20): 4777–85. [PubMed: 23562048]
27. Sofou S. Radionuclide carriers for targeting of cancer. Int J Nanomedicine. 2008; 3(2):181–99. [PubMed: 18686778]
28. Bednarczyk, EM. Ann Pharmacother. 3. 2012. Radiopharmaceuticals in Nuclear Pharmacy and Nuclear Medicine.
29. Terman JR, Kashina A. Post-translational modification and regulation of actin. Curr Opin Cell Biol. 2013; 25(1):30–8. [PubMed: 23195437]
30. Metreveli NO, et al. UV-vis and FT-IR spectra of ultraviolet irradiated collagen in the presence of antioxidant ascorbic acid. Ecotoxicol Environ Saf. 2010; 73(3):448–55. [PubMed: 20036425]
31. Miles CA, et al. Identification of an intermediate state in the helix-coil degradation of collagen by ultraviolet light. J Biol Chem. 2000; 275(42):33014–20. [PubMed: 10893225]
32. Fujimori E. Ultraviolet light-induced change in collagen macromolecules. Biopolymers. 1965; 3(2):115–9. [PubMed: 5889539]
33. Sionkowska A, Kaminska A. Thermal helix-coil transition in UV irradiated collagen from rat tail tendon. Int J Biol Macromol. 1999; 24(4):337–40. [PubMed: 10408640]
34. Gluck U, et al. Regulation of adherens junction protein expression in growth-activated 3T3 cells and in regenerating liver. Exp Cell Res. 1992; 202(2):477–86. [PubMed: 1383015]

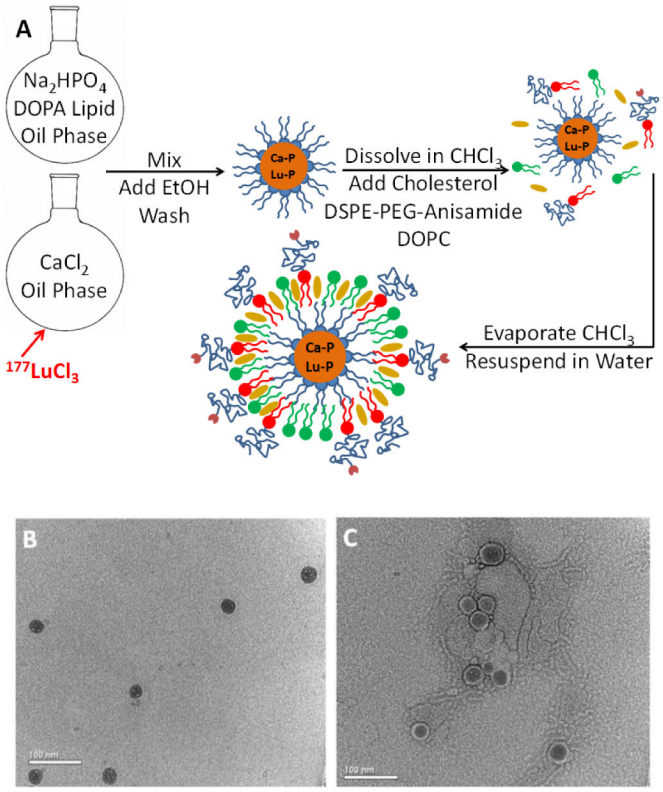

Figure 1.

^{177}Lu-LCP Formulation. A) Schematic depicting general formulation procedure. B) TEM image of final ^{177}Lu-LCP. C) TEM image of final ^{177}Lu-LCP with uranyl acetate negative stain applied. Scale bar represents 100 nm.

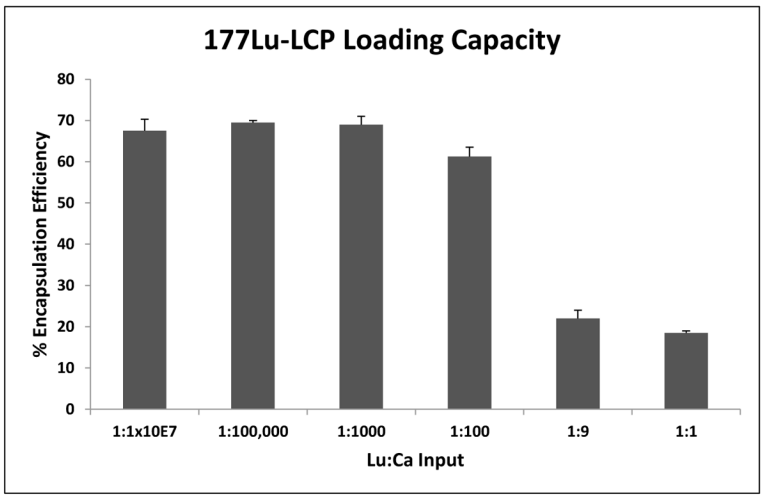

Figure 2.

^{177}Lu-LCP encapsulation efficiencies at increasing levels of lutetium. ^{177}Lu EE decrease begins around 1:100 Lu:Ca. n = 2–3.

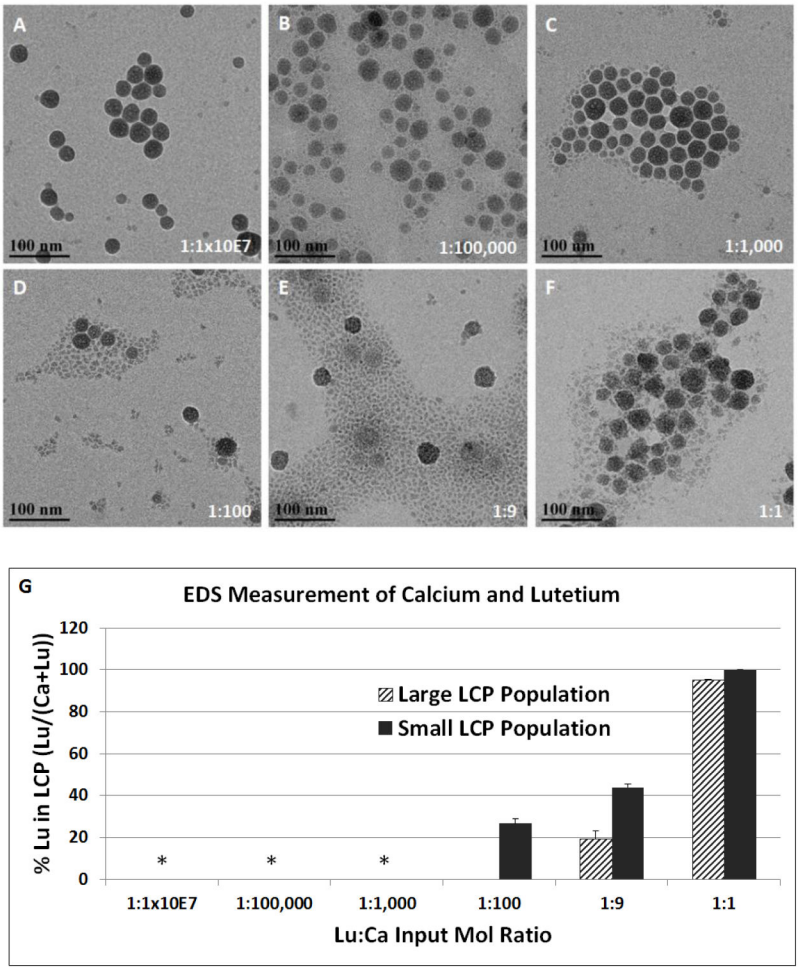

Figure 3.

^{177}Lu-LCP morphologies at different Lu:Ca inputs. A–F) TEM images of ^{177}Lu-LCP at varying Lu inputs. G) Percent Lu in output ^{177}Lu-LCP based on Lu:Ca inputs, calculated by energy dispersive X-ray spectroscopy (EDS). *Lu not detected; negligible small LCP population

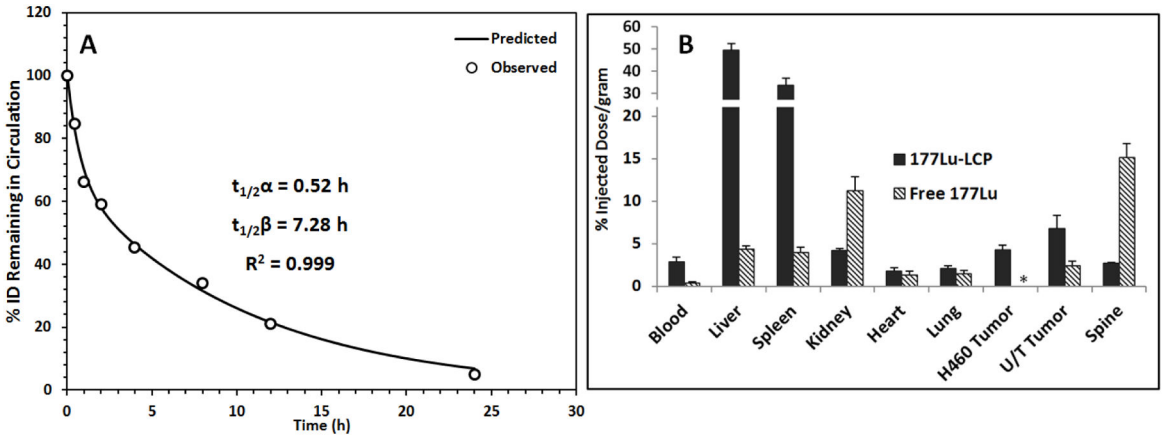

Figure 4.

^{177}Lu-LCP Pharmacokinetics and Biodistribution. A) The PK curve of i.v. injected ^{177}Lu-LCP fit to a two-compartment model; n = 5. B) Organ BD at t = 24h after i.v. injection of ^{177}Lu-LCP or free $^{177}LuCl_3$; n = 3–4. H460 tumor and UMUC3/3T3 (U/T) tumor were subcutaneously inoculated in different mice. *BD of free ^{177}Lu was not tested in H460 tumor-bearing mice.

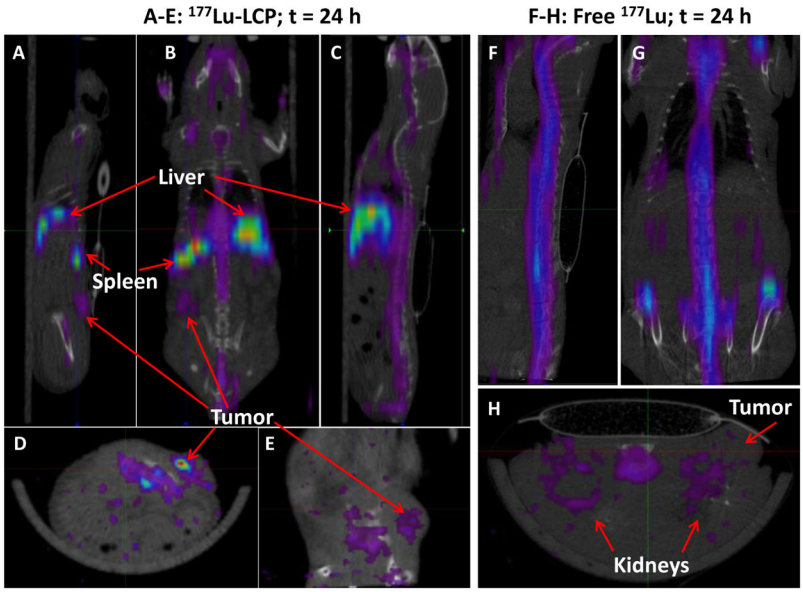

Figure 5.

SPECT/CT images of nude mouse bearing subcutaneous UMUC3/3T3 tumor on left flank at 24 h after injection of ^{177}Lu-LCP (Figures 5A–E) or free ^{177}Lu (Figures 5F–H). Mouse slit collimator was used for whole body imaging: A) left sagittal, B) coronal, C) midsagittal, F) mid-sagittal and G) coronal views. Pinhole collimator was used in D), E), and H) for higher resolution axial and left sagittal views. ^{177}Lu-LCP accumulated in tumor, liver, and spleen, while free ^{177}Lu accumulated in the bone and kidneys, but not in the tumor.

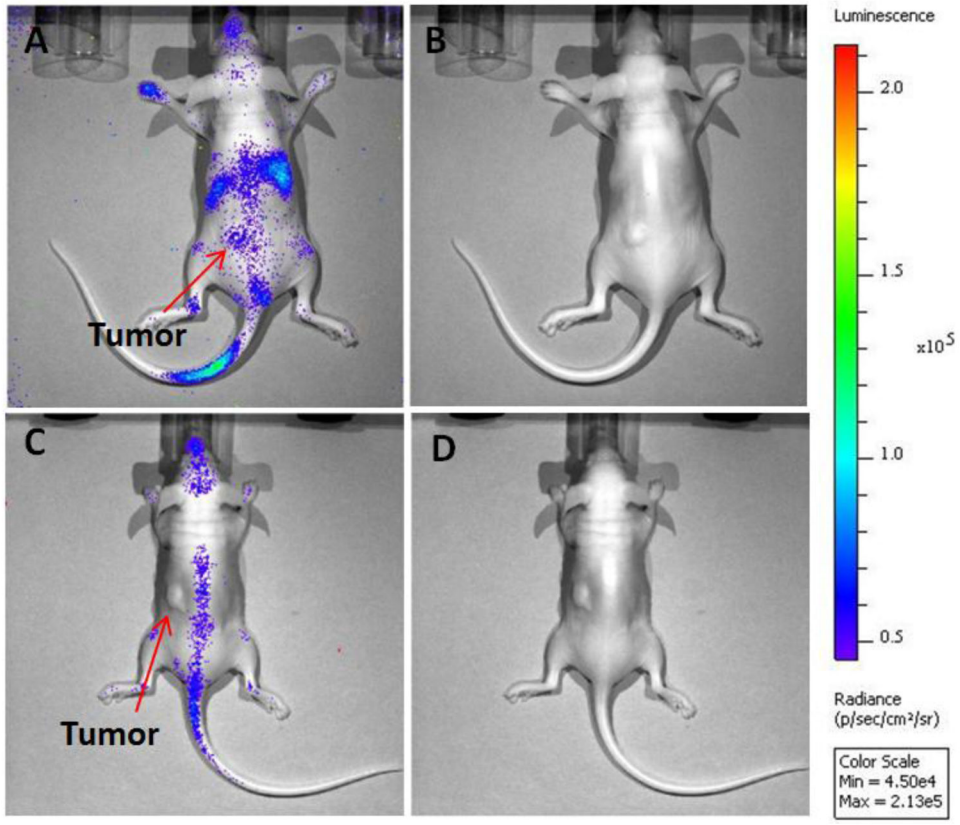

Figure 6.

Images of Cerenkov luminescence in nude mice bearing subcutaneous UMUC3/3T3 tumor on left flank. Luminescence image (A) and plain photograph (B) in mouse 24 h after injection of 2.5 mCi ^{177}Lu-LCP. Luminescence image (C) and plain photograph (D) in mouse 24 h after injection of 2.5 mCi free $^{177}LuCl_3$. Optical images demonstrated ^{177}Lu-LCP accumulation in liver, spleen, and tumor, while free $^{177}LuCl_3$ mainly accumulated in the spine. Data was acquired by an IVIS optical system.

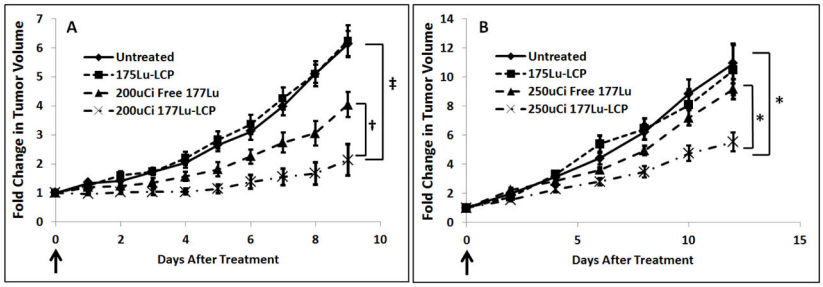

Figure 7.

In vivo tumor growth inhibition in two subcutaneous xenograft tumor models. Nonradioactive ^{175}Lu was loaded into LCP NPs to act as a vehicle control. One dose per mouse was delivered intravenously on Day 0 (arrows). A) Human UMUC3 bladder cancer supplemented with murine 3T3 fibroblasts. B) Human H460 non-small cell lung cancer. Initial tumor sizes ~100–150 mm^3; n = 5–8; †p<0.03, ‡p<5e-5, *p<0.015.

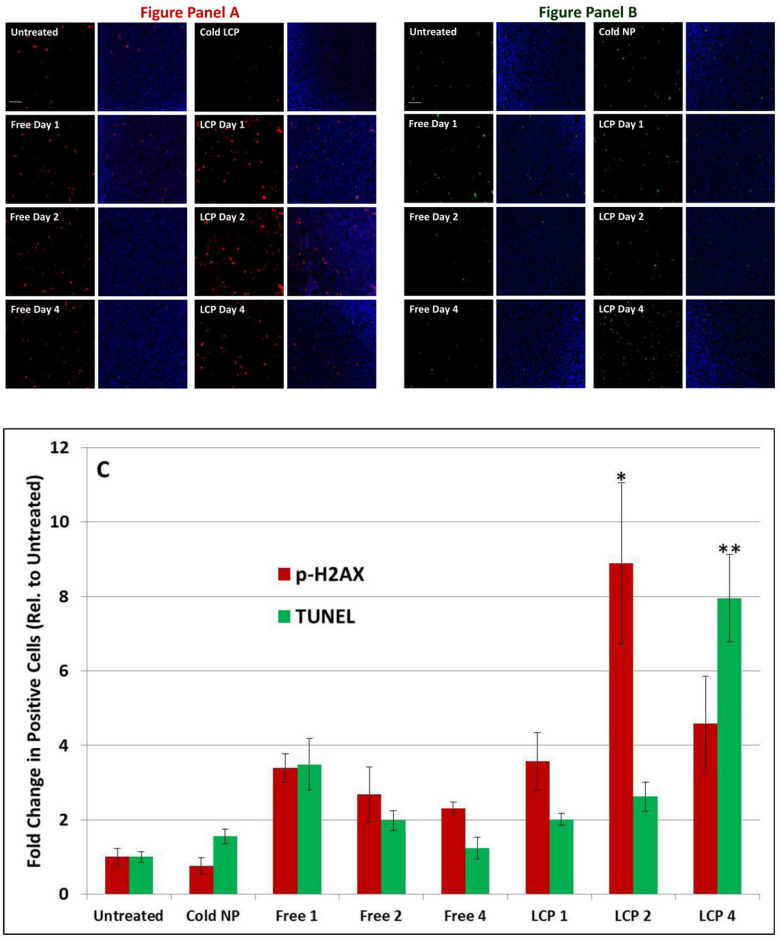

Figure 8.

Cytotoxicity of ^{177}Lu-LCP in vivo: Mice were treated with 200 μCi of ^{177}Lu-LCP or controls and were killed one, two, or four days after administration. Figure panel A shows p-H2AX-positive cells (red) in UMUC3/3T3 tumor sections with or without DAPI (blue). Figure panel B shows TUNEL-positive cells (green) in tumor sections with and without DAPI (blue). Sections in Figure panel B are taken from an adjacent section to those displayed in Figure Panel A. Five representative fields were quantified for TUNEL or p-H2AX-positive cells. Images appearing in Figure panels A and B represent the field with the third-highest quantification. Average values are shown in Figure C: highest p-H2AX upregulation (red) occurred two days after ^{177}Lu-LCP treatment, while highest TUNEL induction (green) occurred 4 days after ^{177}Lu-LCP treatment. *$p < 0.007$; **$p < 0.0005$ compared to control. Scale Bar = 100 μm.

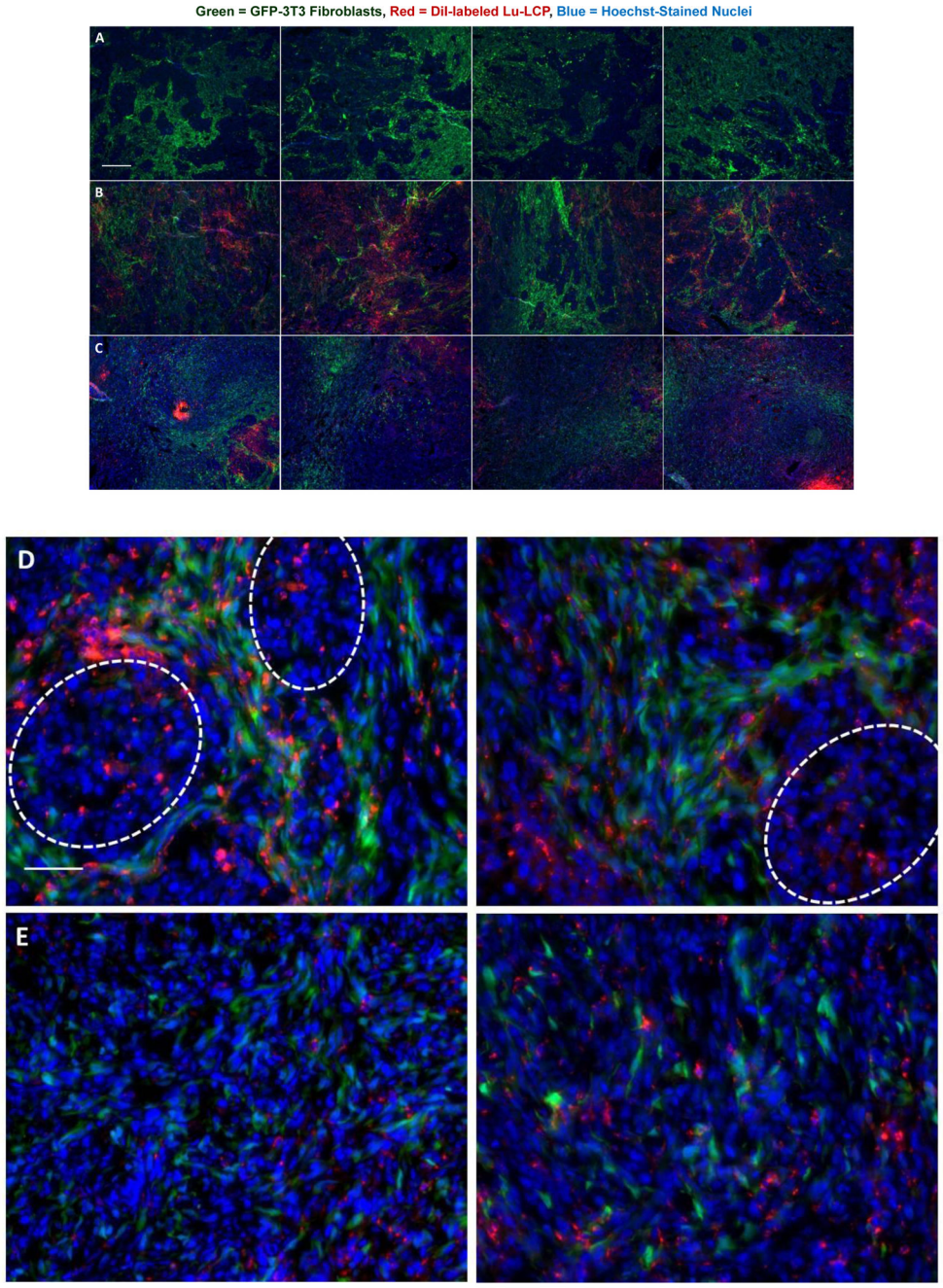

Figure 9.

UMUC3/3T3-GFP (green) tumor sections, with tumor nests outlined in white. Row A) Untreated tumors. Row B) t = 2 days after treatment with cold DiI-^{175}Lu-LCP (red). Row C) t = 2 days after treatment with hot DiI-^{177}Lu-LCP (red). Row D) High magnification images t = 2 days after treatment with cold DiI-^{175}Lu-LCP (red). Row E) High magnification images t = 2 days after treatment with hot DiI-^{177}Lu-LCP (red); disorganized fibroblast structure does not allow tumor nest formation. Each row shows representative photographs from each group, consisting of several tumors and tumor sections. Scale Bar = 300 μm for rows A–C and 50 μm for rows D–E.

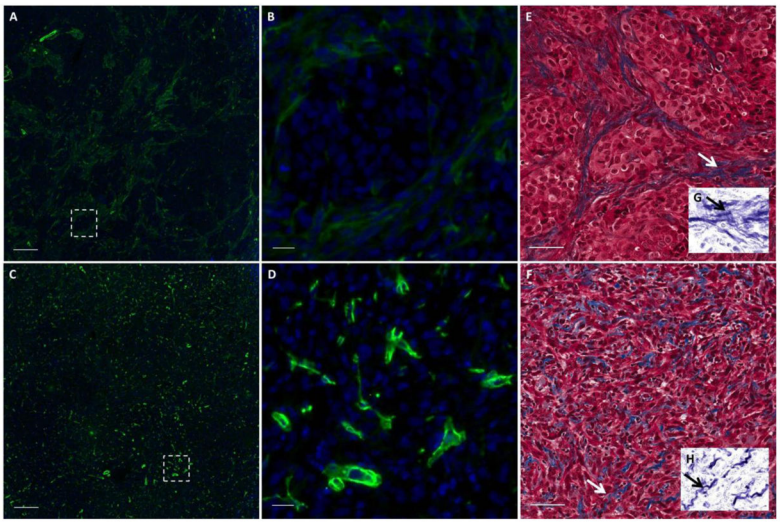

Figure 10.

Microenvironment structure in UMUC3/3T3 tumor sections t = 4 days after treatment with ^{177}Lu-LCP: A–D) Stain for fibroblast marker α-SMA (green) in UMUC3/3T3 tumor sections. Figures A and C show α-SMA expression in an untreated tumor and in a tumor at t = 4 days after treatment with ^{177}Lu-LCP; scale bars = 200 μm. White dashed boxes are zoomed in in Figures B and D; scale bars = 20 μm. E–H) Trichrome stain in tumors that are untreated (E) or t = 4 days after treatment (F). Inserts G–H on bottom right have been processed to show a more isolated view of the collagen stain. Arrows show the location of the region in the insert. Scale bar = 50 μm.

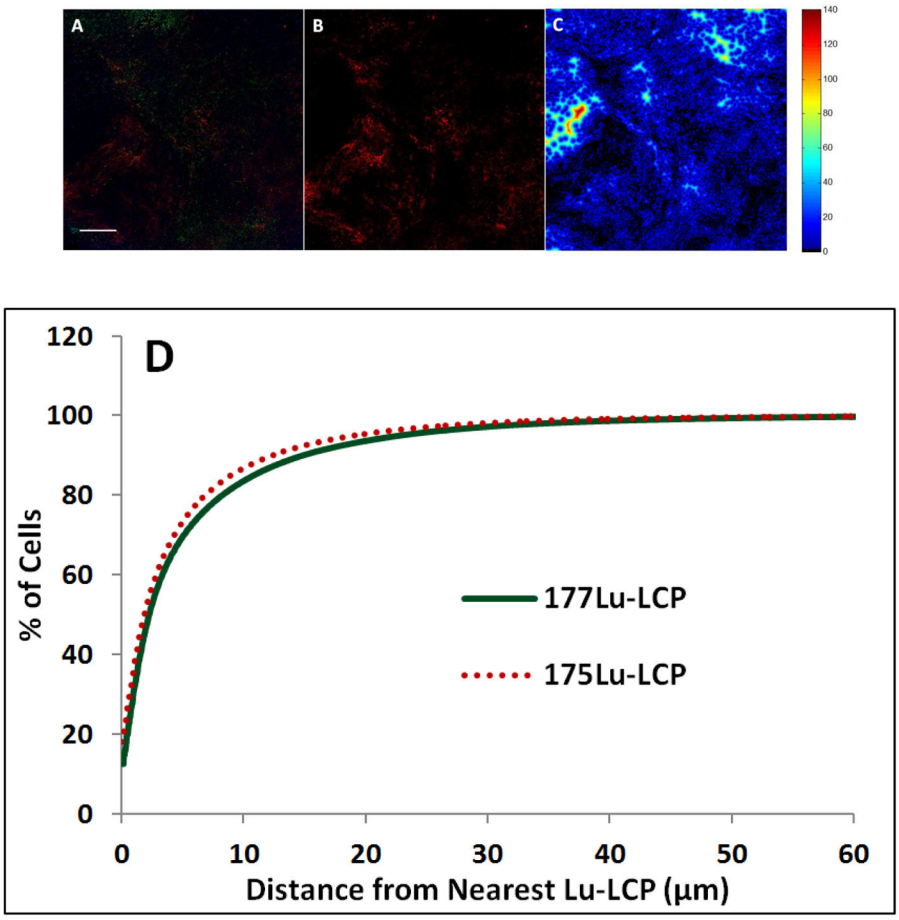

Figure 11.

Quantification of DiI distribution at t = 2 days: A) UMUC3/3T3-GFP tumor given DiI-^{177}Lu-LCP; scale bar = 500 μm; B) Isolated DiI signal from panel A; C) Heat map showing each cell's distance from its nearest Lu-LCP, where black and blue areas show areas of close proximity between cells and particles; D) Quantification of relative cell distance from Lu-LCP; n = 1.75×10^6 cells in 8 sections; n = 4 sections each for ^{177}Lu-LCP and ^{175}Lu-LCP.

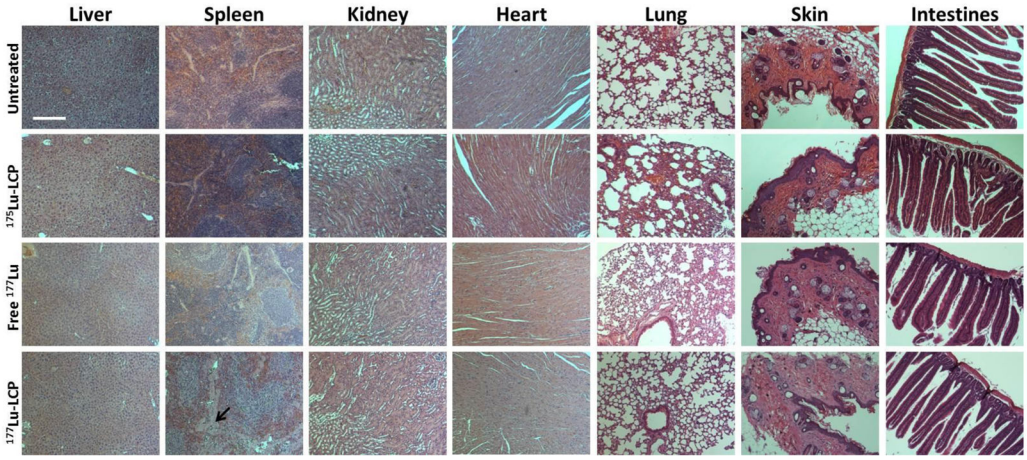

Figure 12.

Healthy nude mouse organs fixed, sectioned, and stained with hematoxylin and eosin 12 days after treatment with 250 μCi ^{177}Lu-LCP or controls to test cumulative toxicity. Some acellular regions (arrow) are visible in spleens treated with ^{177}Lu-LCP. Scale bar = 150 μm.

Table 1

^{177}Lu-LCP inputs and output activity based on a specific activity of 20 Ci/mg of lutetium, the minimum standard for PerkinElmer delivery. Ca is always given at a 5x molar excess of PO_4. Highest level of stable LCP formulation is 1:1000 Lu:Ca. A trace amount of ^{177}Lu was supplemented with nonradioactive ^{175}Lu to achieve the proper Lu:Ca ratio.

Lu:Ca Input (mols)	PO_4 Input (mols)	Total Lu Input (mols)	Input Activity* (mCi)	^{177}Lu EE	Output Activity (mCi)
$1:1\times10^{7}$	2.0×10^{-6}	1.0×10^{-12}	0.0035	0.68	0.0024
1:100,000	”	1.0×10^{-10}	0.354	0.70	0.25
1:1000	”	1.0×10^{-8}	35.4	0.69	24.4
1:100	”	1.0×10^{-7}	354	0.61	217
1:9	”	1.1×10^{-6}	3933	0.22	865
1:1	”	1.0×10^{-5}	35400	0.19	6549

J Control Release. Author manuscript; available in PMC 2016 November 10.

Table 2

Toxicity of ^{177}Lu in mice, measured 12 days after treatment with 250 μCi ^{177}Lu-LCP or controls to test cumulative toxicity: A) Serum protein values in healthy, but immunocompromised, nude mice; B) Serum protein values in healthy CD-1 mice; C) Whole blood analysis in healthy CD-1 mice, measuring white blood cell count (WBC), hematocrit (HCT), mean cell volume (MCV), red blood cell count (RBC), hemoglobin count (HGB), and platelet count (PLT). ^{177}Lu-LCP treatment does not present significant cumulative renal/hepatotoxicity, but causes a decrease in WBC and PLT.

A) Nude Mice	BUN (mg/dL)	Creatinine (mg/dL)	AST (U/L)	ALT (U/L)
Untreated	23 ± 0.5	0.1 ± 0	99 ± 13	37 ± 2
^{175}Lu-LCP	23 ± 1.0	0.1 ± 0	102 ± 2	34 ± 5
250 μCi Free ^{177}Lu	20 ± 1.7	0.1 ± 0	88 ± 16	41 ± 1
250 μCi ^{177}Lu-LCP	24 ± 1.9	0.1 ± 0	73 ± 4	40 ± 4
Normal Range	8–33	0.2–0.9	54–298	17–77

B) CD-1 Mice	BUN (mg/dL)	Creatinine (mg/dL)	AST (U/L)	ALT (U/L)
Untreated	20 ± 0.3	0.1 ± 0	69 ± 14	33 ± 1
^{175}Lu-LCP	21 ± 1.3	0.2 ± 0.03	91 ± 12	35 ± 2
250 μCi Free ^{177}Lu	15 ± 0.7	0.1 ± 0	109 ± 15	41 ± 3
250 μCi ^{177}Lu-LCP	15 ± 0.5	0.1 ± 0	125 ± 9	45 ± 5
Normal Range	8–33	0.2–0.9	54–298	17–77

C) CD-1 Mice	WBC (10^3/μl)	HCT (%)	MCV (fl)	RBC (10^6/μl)	HGB (g/dl)	PLT (10^3/μl)
Untreated	4.5 ± 0.2	52.6 ± 0.2	48.9 ± 0.2	10.7 ± 0.1	16.3 ± 0.1	892 ± 36
^{175}Lu-LCP	5.2 ± 0.7	50.6 ± 1.1	51.0 ± 1.4	10.0 ± 0.5	15.7 ± 0.3	679 ± 54
250 μCi Free ^{177}Lu	2.3 ± 0.4	47.6 ± 1.7	53.8 ± 3.8	8.9 ± 0.4	14.6 ± 0.3	926 ± 34
250 μCi ^{177}Lu-LCP	0.3 ± 0.1	38.8 ± 2.2	50.5 ± 1.6	7.7 ± 0.4	12.0 ± 0.6	217 ± 24
Normal Range	2.6 – 10.1	32.8 – 48.0	42.3 – 55.9	6.5 – 10.1	10.1 – 16.1	780 – 1540